PHYSICAL REVIEW E **91**, 043012 (2015)

Multirelaxation-time lattice Boltzmann model for droplet heating and evaporation under forced convection

Daniel Albernaz,[*] Minh Do-Quang, and Gustav Amberg
Linné Flow Center, Department of Mechanics, The Royal Institute of Technology, Stockholm, Sweden

(Received 19 September 2014; published 21 April 2015)

We investigate the evaporation of a droplet surrounded by superheated vapor with relative motion between phases. The evaporating droplet is a challenging process, as one must take into account the transport of mass, momentum, and heat. Here a lattice Boltzmann method is employed where phase change is controlled by a nonideal equation of state. First, numerical simulations are compared to the D^2 law for a vaporizing static droplet and good agreement is observed. Results are then presented for a droplet in a Lagrangian frame under a superheated vapor flow. Evaporation is described in terms of the temperature difference between liquid-vapor and the inertial forces. The internal liquid circulation driven by surface-shear stresses due to convection enhances the evaporation rate. Numerical simulations demonstrate that for higher Reynolds numbers, the dynamics of vaporization flux can be significantly affected, which may cause an oscillatory behavior on the droplet evaporation. The droplet-wake interaction and local mass flux are discussed in detail.

DOI: 10.1103/PhysRevE.91.043012 PACS number(s): 47.55.−t, 47.11.−j, 64.70.fm, 05.70.Fh

I. INTRODUCTION

Droplet evaporation is of extensive importance to many scientific and technical applications. Examples can be found in natural processes (e.g., the dynamics of raindrops and fog) or in industry such as spray drying, fuel injection in combustion engines, and gas turbines. Evaporation involves phase change where coupling of heat and mass transport is required. Therefore, the complexity in interfacial dynamics is challenging when it comes to numerical simulations. The classical numerical schemes for computing interface motion are the tracking method and the capturing approach. The first was used by Renksizbulut and Yuen [1] with the moving mesh method to simulate droplet evaporation, where variable properties on evaporation were also investigated [2]. Haywood *et al.* [3] used a similar model where deformed droplets are considered.

Regarding the interface-capturing approach, different methods have been applied to investigate droplet evaporation. Tanguy *et al.* [4] developed a level-set method associated with the ghost fluid method to enable higher-order discretization schemes at the interface. Zhang [5] and Balaji *et al.* [6] used a finite-volume method where the droplet maintains a spherical shape. A volume of fluid method (VOF) was used by Hase and Weigand [7,8] where strong deformations are captured. Schlottke and Weigand [9] improved the same VOF code to perform direct numerical simulations of droplet evaporation. VOF was also used by Strotos *et al.* [10] and Banerjee [11] where a multicomponent droplet was considered.

Although each method has a different approach, it is necessary to impose accurate jump conditions across the interface to satisfy energy, momentum, and mass conservation. In order to do so, conservations conditions must be satisfied and a local vaporizing mass flow rate is explicitly defined. An evaporation model often introduces different simplifications, e.g., nondeformable droplet (axisymmetric evaporation) or the assumption of constant gas physical properties (quasisteady). The authors recommend reviews by Sazhin [12] and Erbil [13] for detailed description of droplet evaporation models.

Molecular dynamics and the lattice Boltzmann method (LBM) are two methods where no tracking method is needed for generating an interface. The first has been focused on studying evaporation of a nanometer-size droplet into its own vapor [14–19]. However, only a static droplet case was investigated due to limitations of the method. The LBM presents a wider range of applications as it is based on mesoscopic kinetic equations, where the macroscopic dynamics of a fluid is the result of the collective behavior of many microscopic particles [20]. The LBM is especially convenient for simulating multiphase flows since a diffuse interface can be obtained.

A common multiphase model used in the LBM was proposed by Shan and Chen [21], where phase separation is induced by imposing short-range intermolecular interaction based on a potential function. The original model has some drawbacks such as large spurious currents for significant density ratio and the stability problem. Different approaches have been used to solve these issues. In particular, Kupershtokh *et al.* [22] developed the exact difference method (EDM) as a new way to incorporate the pseudopotential force into LBM multiphase simulations. The spurious currents produced at the vapor-liquid interface are substantially reduced and the method is more stable, where the unphysical phenomenon of relaxation time dependence is avoided [23]. The Bhatnagar-Gross-Krook (BGK) [24] model is a widely used collision operator due to its simplicity, with a single relaxation time. However, for higher Reynolds number (achieved for low values of fluid viscosity), the model is numerically unstable. A remedy is to use a multiple relaxation time (MRT) model [25,26] where the growth of numerical instabilities is reduced.

Thermodynamic effects with phase change have been considered in the LBM perspective by different schemes [27–31]. Droplet evaporation was first investigated by Palmer and Rector [32] with a free-energy model. However, their algorithm could not be used for thermally driven phase changes as pointed out later by the authors [33]. Safari *et al.* [34] used a phase-field method to simulate a static droplet evaporation with large density ratio. Similarly to the VOF method, the liquid and gas are considered immiscible and incompressible

---

[*] daniel@mech.kth.se

where the mass transfer rate through the interface is given by a source term. The energy equation is solved only for the gas phase where a cutoff is needed at the interface, which noticeably influences the evaporative mass flux. Recently, Ledesma-Aguilar *et al.* [35] studied droplet evaporation driven by a concentration gradient but considering a sessile droplet and planar film.

In the present work, we consider a MRT-EDM scheme to simulate the heating and vaporization of a droplet into its own vapor under forced convection. Despite different multiphase models with MRT having been suggested [36,37], the EDM forcing scheme has the advantage of coupling with the MRT model independently, as the forcing scheme shows no dependence with the relaxation times [38]. To the best of our knowledge the thermal phase change for the MRT-EDM is a subject still unexplored in the LBM context. Among the thermal LBM categories [31], we employ the double distribution function (DDF) approach [39], which exhibits good numerical stability and adjustable Prandtl number. The DDF uses one distribution function to represent the density and velocity fields and another for the temperature field, which is advected passively by the fluid flow. Therefore, the coupling between energy and momentum is done at the macroscopic level.

This paper is organized as follows. In Sec. II the model formulation is introduced. Results and discussion are presented in Sec. III. We first validate the method for a static droplet and proceed with numerical results for a droplet under forced convection. The wake-droplet interaction and evaporation dependence on convection and temperature gradient are presented. Local mass flux and liquid circulation driven by surface shear are also analyzed. Finally, brief conclusive remarks will be given in Sec. IV.

II. LATTICE BOLTZMANN METHOD

In this section, a two-dimensional nine-velocity (D2Q9) thermal LBM is presented. The MRT collision operator and EDM pseudopotential force are described. We then introduce the energy equation, based on a passive scalar approach.

A. The MRT model

The equation for the flow field is provided in terms of a discrete Boltzmann equation, given by

$$f_i(\mathbf{x}+\mathbf{c}_i\delta_t, t+\delta_t) = f(\mathbf{x},t) + \delta_t\Omega_i + \delta_t F_i', \tag{1}$$

where f_i is the density distribution function, t is time, and δ_t is the time step. The lattice velocity is given by $\mathbf{c}_i$, $\mathbf{x}$ is the spatial position, and F' is the external forcing term in the velocity space. The change of f_i due to collisions is represented by Ω_i. The discrete velocity vectors are written as

$$\mathbf{c}_i = \begin{cases} (0,0), \\ i=0 \\ (\cos[(i-1)\pi/2], \sin[(i-1)\pi/2])c, \\ i=1-4 \\ (\cos[(2i-9)\pi/4], \sin[(2i-9)\pi/4])c, \\ i=5-8, \end{cases}$$

where $c_{\text{ref}} = \delta_x/\delta_t$, δ_x being the lattice spacing. The length is scaled using δ_x and time is made dimensionless using the time step δ_t, where $c_{\text{ref}} = 1$ and the speed of sound is defined as $c_s = 1/\sqrt{3}$. The collision operator for the MRT model is defined as

$$\Omega_i = (\mathbf{M}^{-1}\mathbf{S}\mathbf{M})_{ij}\left[f_j(\mathbf{x},t) - f_j^{\text{eq}}(\mathbf{x},t)\right], \tag{2}$$

where $\mathbf{M}$ is the orthogonal transformation matrix [25], f_j^{eq} is the equilibrium distribution function, and $\mathbf{S}$ is a non-negative diagonal relaxation matrix, given by

$$\mathbf{S} = \text{diag}(s_\rho, s_e, s_\epsilon, s_j, s_q, s_j, s_q, s_\nu, s_\nu), \tag{3}$$

where $0 < s_i < 2$ and $s_\nu = 1/\tau_f$, τ_f being the relaxation time related to the kinematic viscosity $\nu = c_s^2(\tau_f - 1/2)$. The distribution f_j can be linearly mapped in the moment space as $\mathbf{m} = \mathbf{Mf}$. The equilibrium f_j^{eq} assumes

$$\mathbf{m}^{\text{eq}} = \mathbf{M}\mathbf{f}^{\text{eq}} = \rho\big(1, -2+3|\mathbf{u}^{\text{eq}}|^2, 1-3|\mathbf{u}^{\text{eq}}|^2, u_x^{\text{eq}}, -u_x^{\text{eq}}, u_y^{\text{eq}}, -u_y^{\text{eq}}, \left(u_x^{\text{eq}}\right)^2 - \left(u_y^{\text{eq}}\right)^2, u_x^{\text{eq}}u_y^{\text{eq}}\big)^T. \tag{4}$$

The density ρ and equilibrium velocity $\mathbf{u}^{\text{eq}}$ are calculated by

$$\rho = \sum_i f_i\ , \quad \mathbf{u}^{\text{eq}} = \frac{1}{\rho}\sum_i \mathbf{c}_i f_i. \tag{5}$$

B. EDM forcing scheme

Kupershtokh and Medvedev [22] derived the EDM for LBM in the form

$$F_i' = f_i^{\text{eq}}(\rho, \mathbf{u}^{\text{eq}} + \Delta\mathbf{u}^{\text{eq}}) - f_i^{\text{eq}}(\rho, \mathbf{u}^{\text{eq}}), \tag{6}$$

where $\Delta\mathbf{u}^{\text{eq}} = \mathbf{F}/\rho$, with $\mathbf{F} = (F_x, F_y)$ being the interparticle interaction force. The EDM forcing scheme can be rewritten as [40]

$$F_i' = \omega_i\left[\frac{\mathbf{c}_i\cdot\mathbf{F}}{c_s^2} + \frac{(\mathbf{c}_i\cdot\mathbf{v})(\mathbf{c}_i\cdot\mathbf{F})}{c_s^4} - \frac{\mathbf{v}\cdot\mathbf{F}}{c_s^2}\right]. \tag{7}$$

Here $\omega_0 = 4/9$, $\omega_{1-4} = 1/9$, and $\omega_{5-8} = 1/36$. The actual fluid velocity is denoted by $\mathbf{v}$, given as

$$\mathbf{v} = \mathbf{u}^{\text{eq}} + \frac{\mathbf{F}}{2\rho}, \tag{8}$$

where $\mathbf{v}$ is taken at half time step, i.e., averaging the momentum before and after collision. It is important to note that Eq. (7) shows no dependence with the relaxation time τ_f. Lycett-Brown and Luo [38] recently showed that the error associated with the EDM force term truncated at second order is independent of τ_f. Therefore, unlike other methods (e.g., Shan-Chen model), the EDM does not influence the collision operator and can be implemented independently of MRT, i.e., Eq. (7) is kept in the velocity space.

Interparticle force methods present spurious currents around the interface that may introduce significant errors which limit the density ratio [41,42]. In order to improve this, Kupershtokh *et al.* [43] suggested a numerical approximation for the local force based on a linear combination of the local and the mean value gradient approximations, calculated by

$$\mathbf{F} = A\sum_{i=1}^{8}\lambda_i\Phi^2(\mathbf{x}+\mathbf{c}_i)\mathbf{c}_i + (1-2A)\Phi(\mathbf{x})\sum_{i=1}^{8}\lambda_i\Phi(\mathbf{x}+\mathbf{c}_i)\mathbf{c}_i, \tag{9}$$

where coefficients λ_i are $\lambda_{1-4} = 4/12$ and $\lambda_{5-8} = 1/12$ and A is a correlative fitting parameter defined by Kupershtokh *et al.*, where a better fit with the coexistence curve can be obtained and a significant decrease in the magnitude of the spurious currents is observed. The special function Φ is written in the form

$$\Phi = \sqrt{\rho c_s^2 - \kappa p}, \tag{10}$$

where κ sets the thickness of the interface, l_i, which is evaluated following Jacqmin [44]. The surface tension is denoted as σ. The pressure is written as p, given by an equation of state (EOS). The Peng-Robinson (PR) EOS is suitable to investigate hydrocarbon droplets evaporating under a high-pressure and -temperature environment [6] and is expressed as

$$p = \frac{\rho R T}{1 - b\rho} - \frac{a\rho^2 \alpha'(T)}{1 + 2b\rho - b^2\rho^2}, \tag{11}$$

with $a = 0.45724 R^2 T_c^2 / p_c$ and $b = 0.0778 R T_c / p_c$, where the subscript c denotes the evaluation at the critical point. The parameter $\alpha'(T) = [1 + (0.37464 + 1.54226w - 0.26992w^2)(1 - \sqrt{T/T_c})]^2$ is defined according to the acentric factor w and the actual temperature T. For the PR EOS, a value of $A = -0.07$ has been shown to yield an accurate reproduction of the coexistence curves in comparison to pure local or pure mean value approximations.

C. Energy equation

A second distribution function is used for solving the energy equation through a passive scalar temperature and is given by

$$g_i(\mathbf{x} + \mathbf{c}_i\delta_t, t + \delta_t) = g_i(\mathbf{x}, t) - \frac{1}{\tau_g}\left(g_i - g_i^{\mathrm{eq}}\right) + G_i, \tag{12}$$

where G_i is a correction term and g_i^{eq} denotes the equilibrium distribution function. A D2Q9 lattice is also used for solving Eq. (12). The collision operator is based on a single relaxation time τ_g, i.e., BGK type [24]. Here the temperature is evaluated by

$$T = \sum_i g_i. \tag{13}$$

The equilibrium function is written as

$$g_i^{\mathrm{eq}} = \omega_i T (1 + 3\mathbf{c}_i \cdot \mathbf{v}). \tag{14}$$

The correction term G_i for Eq. (12) in dimensionless form is proposed as

$$G_i = \omega_i \left[\frac{\nabla \cdot (K \nabla T_r)}{\rho_r c_{p,r}} - \alpha^{\mathrm{LB}} \nabla^2 T_r\right] + \omega_i T_r \left[1 - \frac{\gamma}{\rho_r c_{p,r}} \left(\frac{\partial p_r}{\partial T_r}\right)_{\rho_r}\right] \nabla \cdot \mathbf{v}. \tag{15}$$

The subscript r denotes the reduced variables, i.e., actual quantity normalized by the critical value (subscript c). The reference length, time, and velocity are the lattice units (l.u.) δ_x, δ_t, and c_{ref}, as used in Sec. II A. Some authors have suggested similar approaches for the correction term G_i [23,28]; however, we employ different considerations for the thermal conductivity. The dimensionless thermal conductivity is denoted as K with the reference value given by $\rho_c c_{p,c} \delta_x^2 / \delta_t$ [45], where c_p is the specific heat at constant pressure. The thermal diffusivity is therefore defined as $\alpha = K/(\rho_r c_{p,r})$, while $\alpha^{\mathrm{LB}} = (\tau_g - 1/2)/3$ is the lattice thermal diffusivity. Reduced variables are used for the remaining quantities. The dimensionless number γ is

$$\gamma = \frac{p_c}{\rho_c c_{p,c} T_c}. \tag{16}$$

Through the Chapman-Enskog expansion, the macroscopic energy equation obtained from Eq. (12) assumes [28]

$$\partial_t T_r + \mathbf{v} \cdot \nabla T_r = \frac{\nabla \cdot (K \nabla T_r)}{\rho_r c_{p,r}} - \frac{T_r \gamma}{\rho_r c_{p,r}} \left(\frac{\partial p_r}{\partial T_r}\right)_{\rho_r} \nabla \cdot \mathbf{v}. \tag{17}$$

In order to simplify the text, the subscript r will be omitted and all the variables are considered by their respective reduced quantities unless otherwise stated. The thermal conductivity changes according to the density and can be written as

$$K = K_\ell \frac{\rho - \rho_v}{\rho_\ell - \rho_v} + K_v \frac{\rho_\ell - \rho}{\rho_\ell - \rho_v}, \tag{18}$$

where ℓ denotes the liquid phase and v the vapor phase. The remaining terms introduced by the correction force need a finite-difference scheme in order to calculate the gradient and Laplacian of a quantity ζ, given respectively by

$$\nabla \zeta(\mathbf{x}) = \sum_i \lambda_i \zeta(\mathbf{x} + \mathbf{c}_i)\mathbf{c}_i, \tag{19}$$

$$\nabla^2 \zeta(\mathbf{x}) = \frac{1}{6}\left[4 \sum_{i=1}^{4} \zeta(\mathbf{x} + \mathbf{c}_i) + \sum_{i=5}^{8} \zeta(\mathbf{x} + \mathbf{c}_i) - 20\zeta(\mathbf{x})\right], \tag{20}$$

where a D2Q9 lattice is still required to maintain higher accuracy and isotropy up to leading order error [46]. Some further considerations can be made for the present model. It is known that the discontinuous phase transition between liquid and vapor can be described with the Clausius-Clapeyron relation, given by

$$\frac{dP}{dT} = \frac{\Delta s}{\Delta v}, \tag{21}$$

where Δs and Δv are the change in specific entropy and specific volume, respectively. The specific latent heat L can be explicitly reconciled by combining the definition $L = T\Delta s$ with Eq. (21), obtaining

$$L = T \frac{dP}{dT}(v_v - v_\ell), \tag{22}$$

where v_v and v_ℓ are the specific volume for the vapor and liquid. Using the EOS in Eq. (11) and for a certain temperature, the latent heat in our model can be evaluated through the right-hand side of Eq. (22). The latent heat is also normalized by its critical value, L_c. One should also note that the resulting diffusive term in Eq. (15) has to be positive for stability reasons. This can be achieved when $\tau_g \to 0.5$, which is a convection-dominant energy problem, where the use of the simplified collision operator BGK is preferable [47].

The MRT model has also been applied to the energy equation (e.g., Ref. [48]); however, it was not necessary to the present case. An alternative way of solving the energy equation is by means of a finite-difference scheme, known as a hybrid approach [49]. The main difference between the DDF and hybrid approaches is that while the first is solved by an auxiliary LB model, the second is solved directly in the macroscopic level. We choose the DDF due to its simplicity.

III. RESULTS AND DISCUSSION

A. Static droplet

In order to validate the proposed model, we simulate a static droplet suspended in vapor. First, an equilibrium condition is used, where there is no occurrence of evaporation. A 300 × 300 lattice with periodic boundary conditions is implemented. A droplet of initial radius $R_0(\mathbf{x}_c) = 40$ is positioned at the center $\mathbf{x}_c$ of the domain. The density field is initialized according to

$$\rho(\mathbf{x}) = \frac{\rho_\ell + \rho_v}{2} - \frac{\rho_\ell - \rho_v}{2} \tanh\left[\frac{2(r|\mathbf{x} - \mathbf{x}_c| - R_0)}{W}\right], \quad (23)$$

where W is a initial interface thickness to facilitate equilibrium and r is the distance to the center. We observe that the parameter W establishes the initial density distribution around the interface and only influence the time taken for the droplet to reach an equilibrium condition. The parameter κ is responsible for defining the interface thickness and is independent of W. In our simulations, we set $W = 7$.

Hexane is the fluid considered, which has an acentric factor $w = 0.30075$. The parameter $\gamma = 0.0094$ is kept constant as it depends only on critical properties. The fixed relaxation times are chosen as $s_\rho = s_j = 1$, $s_e = s_\epsilon = 0.8$, and $s_q = 1.1$. For the energy equation, $\tau_g = 0.53$.

Figure 1 shows the coexistence curve obtained in the numerical simulations as a function of the saturated temperature T_{sat}. A comparison is made with the Maxwell construction rule for the PR EOS, using hexane, and good agreement is observed when $A = -0.07$. Here, the interface is considered when $\rho_i = (\rho_\ell + \rho_v)/2$, where the subscript i refers to quantities evaluated at the interface.

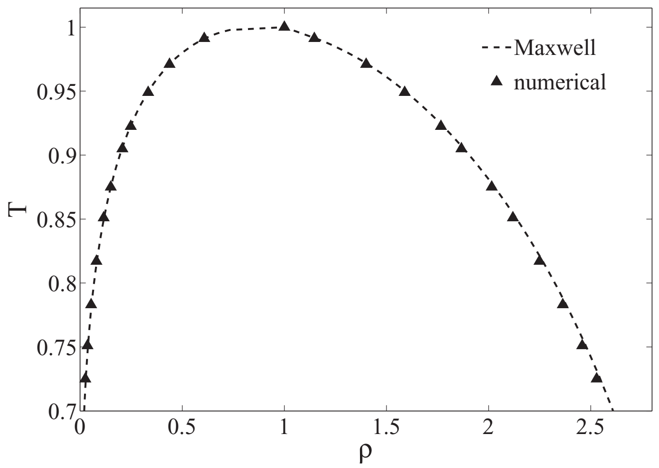

FIG. 1. Comparison of saturated vapor and liquid branches between the Maxwell construction and results obtained from our numerical model. A hexane hydrocarbon is considered for the PR EOS. For simulations, the parameters are $A = -0.07$, $\tau_f = 0.5208$, and $\kappa = 0.010$.

TABLE I. Physical properties according to the reduced temperature T_{sat}, relaxation time τ_f, and κ.

Case	T_{sat}	τ_f	κ	σ	l_i (l.u.)	$\text{v}_{\max}$	ρ_ℓ/ρ_v
1	0.80	0.5813	0.010	0.1030	5	$4.9e-4$	36.5
2	0.85	0.5813	0.005	0.1208	11	$1.1e-4$	19.4
3	0.85	0.5813	0.010	0.0852	6	$3.8e-4$	19.6
4	0.85	0.5208	0.010	0.0850	6	$2.1e-3$	19.6
5	0.90	0.5813	0.010	0.0468	8	$1.3e-4$	9.9

The influence of the parameters T_{sat}, τ_f, and κ are listed in Table I. Surface tension is obtained by Laplace's law (detailed validation can be found in Albernaz *et al.* [50]). The increase of κ produces a thinner interface thickness l_i where surface tension is weaker. The maximum velocity $\text{v}_{\max}$, which represents the spurious currents in the equilibrium condition, is enhanced either by a thinner interface or by reducing the relaxation time τ_f.

We observe that the density ratio ρ_ℓ/ρ_v is independent of τ_f for the same T and κ. Furthermore, for lower values of τ_f the computational time needed to achieve equilibrium is raised. When T_{sat} increases, for the same κ, the interface is thicker, which is expected as it gets closer to the critical point. It is important to mention that if a BGK model is employed to simulate the same static droplet with the relaxation times used in Table I, the computations become unstable.

The dynamics of phase change had also to be validated, which is done by means of a static radial droplet evaporation only due to diffusion. An analytical solution for the droplet evaporation rate can be obtained and compared to the numerical results. The one-component equation of transport of heat in cylindrical coordinates is given by:

$$r\rho c_p \text{v}_r \frac{\partial T}{\partial r} = \frac{\partial}{\partial r}\left(rk\frac{\partial T}{\partial r}\right). \quad (24)$$

The energy balance at the interface is given by the boundary condition [51]

$$k_v \frac{dT}{dr}\bigg|_{i,v} = k_\ell \frac{dT}{dr}\bigg|_{i,\ell} + \rho_i \text{v}_i L_{hv} = \rho_i \text{v}_i L_{\text{eff}}. \quad (25)$$

The latent heat of vaporization is denoted by L_{hv}, whereas the effective latent heat of vaporization is L_{eff}. The temperature of the droplet is generally considered constant, as the transport of heat inside the droplet is negligible, i.e., $L_{\text{eff}} = L_{hv}$, which is also assumed in order to obtain the analytical solution. Using the continuity equation $r\rho\text{v} = r_i\rho_i\text{v}_i$ and Eq. (25) we integrate Eq. (24) with respect to r, which gives

$$r_i\rho_i\text{v}_i c_p\left(T - T_i + \frac{L_{hv}}{c_p}\right) = rk\frac{dT}{dr}. \quad (26)$$

After separating the variables we integrate Eq. (26) within the intervals $[r_i, r_\infty]$ and $[T_i, T_\infty]$, obtaining

$$r_i\text{v}_i \ln(r_\infty/r_i) = \alpha_i \ln(1 + B), \quad (27)$$

where $B = c_p(T_\infty - T_i)/L_{\text{hv}}$ is the nondimensional Spalding number. Using the mass continuity at the droplet surface $-\rho_\ell dr_i/dt = \rho_i \text{v}_i$ and now integrating for r and t, for an initial diameter D_0, we have the diameter D evolution in time as

$$D^2\left[\frac{1}{2} + \ln\frac{D_\infty}{D}\right] = c' D_0^2 - \frac{8\alpha_i \rho_i}{\rho_\ell}\ln(1+B)t, \tag{28}$$

where $c' = 1/2 + \ln(D_\infty/D_0)$ is a constant. The same derivation in spherical coordinates is known in the literature as the D^2 law [52].

In order to simulate a static droplet evaporation, the droplet is first equilibrated with the vapor at the saturated temperature in a periodic domain. Then outflow boundaries are used, where the Neumman boundary condition (NBC) is applied to the velocity. The temperature is then gently raised at the boundaries, set by a Dirichlet boundary condition (DBC). To keep the pressure $p(\rho,T)$ constant, density is also set as DBC, calculated by the PR EOS for a given initial pressure and current temperature.

The heat-up of the surrounding vapor, i.e., the conduction of heat through the boundaries to the vapor phase toward the droplet interface, takes $t \sim 5 \times 10^4$. After this heat-up phase, the droplet evaporation is analyzed. We observe that a symmetric radial flow is obtained, where no artificial heating occurs. Consistent droplet evaporation was seen even for relatively high density ratio, $\rho_\ell/\rho_v \cong 130$, for $T_s = 0.7$.

Figure 2 compares the solution of the D^2 law, Eq. (28), and the numerical results from the present model, where $D_0 = 60$, $D_\infty = 300$, $\alpha_i = 0.0223$, and $B = 0.431$. We make use of the parameters defined for cases 2 and 3 in Table I, where only the thickness of the interface is changed. The spurious currents for case 2 is almost 4 times smaller than 3. Nevertheless, we observe that our model is able to produce the correct evaporation rate for both interface thicknesses. Since the static droplet evaporation occurs only due to diffusion, the results indicate that the spurious currents do not influence the evaporation rate. As the droplet shrinks, case 2 shows slight deviation from the D^2 law. This is expected since the interface thickness is of the order of the droplet size, where an overestimation of diffusion occurs. Therefore, it is important to be aware of the accuracy of the results based on the relation between the droplet size and interface thickness.

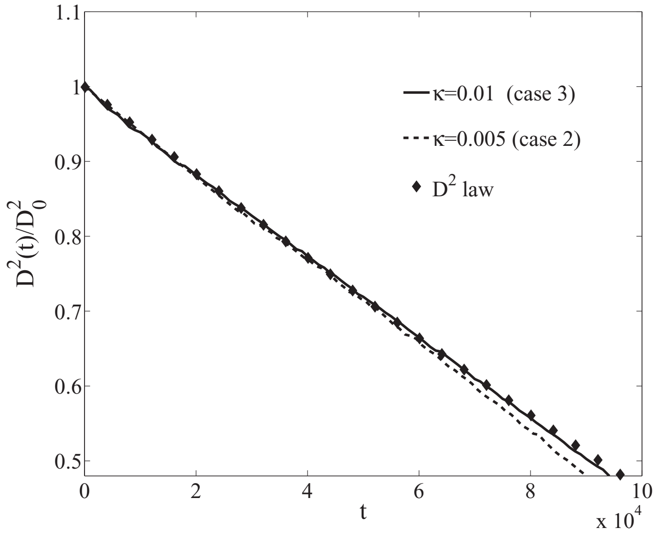

FIG. 2. Normalized square diameter evolution in time, where the D^2 law solution [Eq. (28)] and simulation results are shown for two different interface thicknesses.

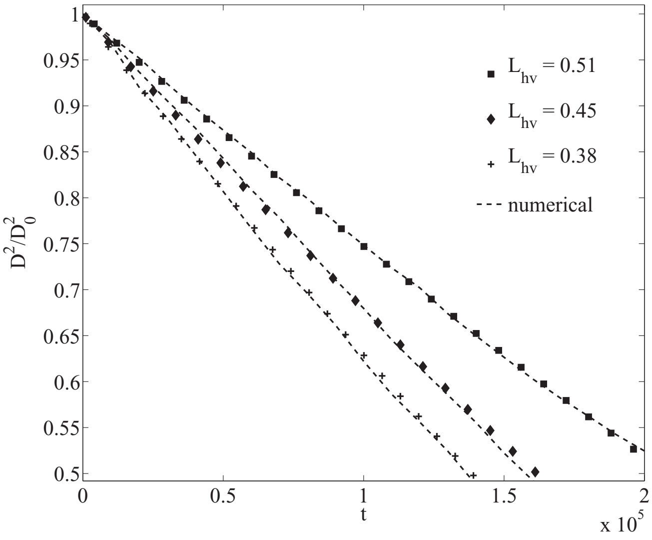

FIG. 3. Comparison between the numerical results and D^2 law of the normalized squared diameter for different latent heat.

It is also important to show that the mass transfer rate in the simulations are consistent with the latent heat, given by the jump condition in Eq. (25) and included in the analytical solution through the Spalding number B. The latent heat L_{hv} is obtained from hexane properties [53], being $L_{\text{hv}}(T = 0.8) = 0.51$, $L_{\text{hv}}(T = 0.85) = 0.45$, and $L_{\text{hv}}(T = 0.9) = 0.38$. First, it was verified that the same L_{hv} is obtained from the Clausius-Clapeyron relation in Eq. (22), with the current Peng-Robinson EOS.

We then compare the square diameter evolution between the numerical results and the D^2 law for different latent heat, shown in Fig. 3. Here the temperature difference is kept the same for all cases, $T_\infty - T_i = 0.1$. The numerical results correspond to cases 1, 3, and 5 and are in accordance with the analytical solutions. It is seen that an increase of L_{hv} is responsible for a slower evaporation. Such behavior is expected as more energy is needed to generate the phase change.

Figure 4 shows the relative error ε between the D^2 law and numerical results as a function of the normalized square diameter. The error is evaluated at the same time step. Different droplet sizes are tested, where the parameters used correspond to case 3 in Table I. We note that good agreement with the D^2 law is obtained, where the smaller droplet $D_0 = 50$ gives $\varepsilon \cong 1\%$ when $D^2/D_0^2 = 0.5$.

B. Evaporation under convective effects

In this section we study the evaporation of a droplet with forced convection. The numerical setup and corresponding boundary conditions are shown in Fig. 5. The top boundary has DBC for the temperature T_∞ and an inlet velocity U.

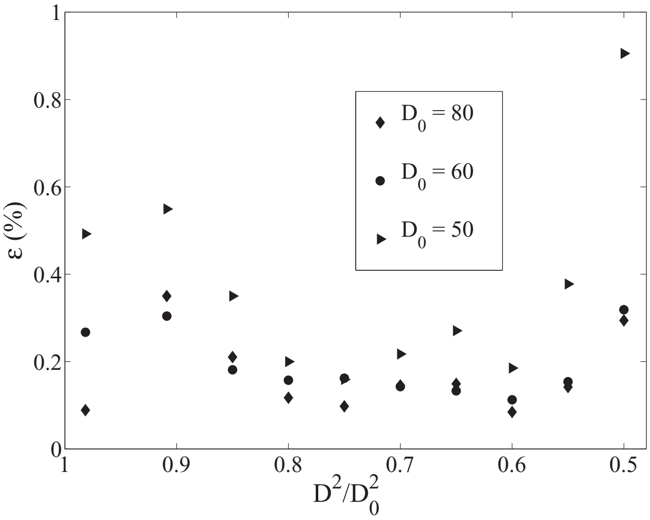

FIG. 4. Error between D^2 law and simulation results for different droplet sizes.

The boundary at the bottom is described with an outflow condition. However, differing from that for pure diffusion, here the pressure assumes $\partial p/\partial n = 0$, n being the normal direction to the boundary. Therefore, NBC are applied for the density and temperature. Periodic condition is used in the x direction.

In the convective case, it is desired that the droplet is kept in the same initial position, as a Lagrangian reference. Experimentally, the droplet is held by a rod while an inflow is set. Numerically, one approach is to estimate the droplet displacement due to the external flow and apply a force on the droplet on the opposite direction of the displacement (e.g., Ref. [54]). We consider a force $F_{d(i)}$, added in Eq. (1) as an external force in the velocity space, similar to the EDM forcing. It is defined based on a spring-damp system and assumes

$$F_{d(i)} = \lambda_i \mathbf{c}_i \cdot [c_1 \mathbf{x}_\delta + c_2 \partial_t \mathbf{x}_d] \times [\rho(\mathbf{x}) - \rho_\infty], \tag{29}$$

where the constants c_1 and c_2 represent control parameters. The term $\mathbf{x}_\delta$ denotes the droplet displacement from the current position $\mathbf{x}_d(t)$ to its initial position $\mathbf{x}_0$, i.e., $\mathbf{x}_\delta = \mathbf{x}_d(t) - \mathbf{x}_0$. The position $\mathbf{x}_d(t)$ is calculated according to the droplet center of mass, where linear interpolation is used at the interface. It is important to note that by using a diffuse interface method, density variation occurs at the interface. Therefore we estimate the counteracting force by relating the droplet displacement with a local density dependence. Therefore, the density difference $\rho(\mathbf{x}) - \rho_\infty$ is included to the force $F_{d(i)}$, which acts only at the droplet.

The control parameters are also evaluated. We observed numerical instabilities when $c_1 > 0.3$. Due to the strong damping, a rigid force is obtained and stronger spurious currents arise. Therefore, c_1 works only for the range $0 \leqslant c_1 \leqslant 0.3$. The constant c_2 is related to the spring behavior, where satisfactory results are seen when $0.15 < c_2 < 1.05$. We verified that for $c_1 = 0.09$ and $c_2 = 0.21$ the force is optimal as it does not influence the evaporation rate nor the magnitude of the spurious currents for a wide range of the inflow velocity.

The Reynolds number is defined as $\mathrm{Re} = UD/\nu$, based on the inlet velocity and droplet diameter. The kinematic viscosity is the same for both phases, which means that the dynamic viscosity ratio μ_ℓ/μ_v is equivalent to the density ratio ρ_ℓ/ρ_v.

A domain by 500 × 500 lattice nodes is considered. The droplet with $D_0 = 60$ is set at the position (250,300) with initial equilibrium temperature $T_{\mathrm{sat}} = 0.85$ and $\kappa = 0.01$. According to the hexane fluid properties for $T = 0.85$ [53], the Prandtl numbers are $\mathrm{Pr}_v = 0.8085$ and $\mathrm{Pr}_\ell = 2.44$ for the vapor and liquid phases, respectively. The relaxation time used is $\tau_f = 0.5813$, which gives $\nu = 0.027$. For achieving the correct Prandtl numbers, we set $\alpha_v = 0.034$ and $\alpha_\ell = 0.011$. No significant change of c_p between different phases is seen when $T = 0.85$, therefore the c_p ratio is assumed to be unity [53].

Numerical simulations are carried out for $\mathrm{Re} = 60$. The corresponding Peclet number is $\mathrm{Pe} = \mathrm{RePr}_v \cong 48.5$ for the vapor phase. We observe that the inlet condition generates a pressure wave that is responsible for increasing the droplet size due to a pressure balance between the droplet and surrounding vapor. The phenomena of a swelling droplet exposed to a higher-pressure environment is well understood in the literature (e.g., Ref. [5]) where evaporation may follow, depending on the ambient temperature. However, our focus is to trigger evaporation only by means of temperature difference instead of variations in pressure.

The direct effect of the flow is the increase of pressure in the entire domain, which corresponds to a shift in the saturated pressure. Therefore, the temperature at the inlet has to be slightly raised to establish an equilibrium condition

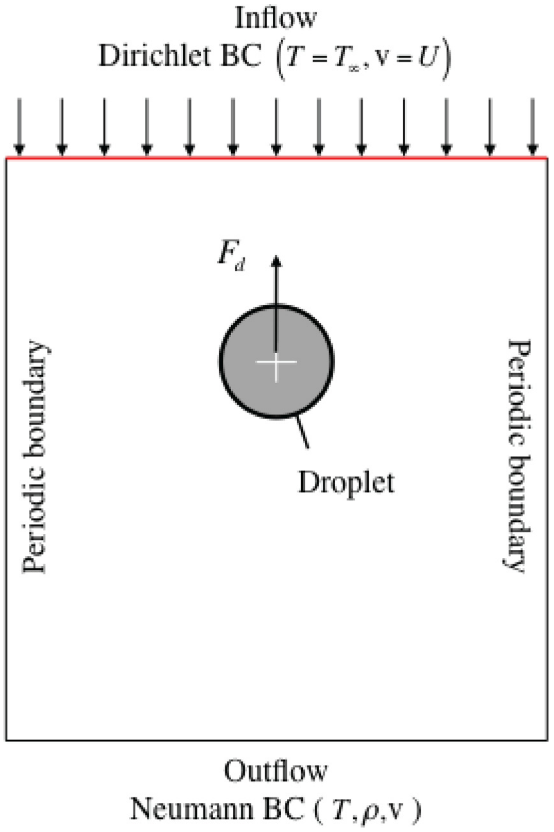

FIG. 5. (Color online) Representation of the computational domain and boundary conditions.

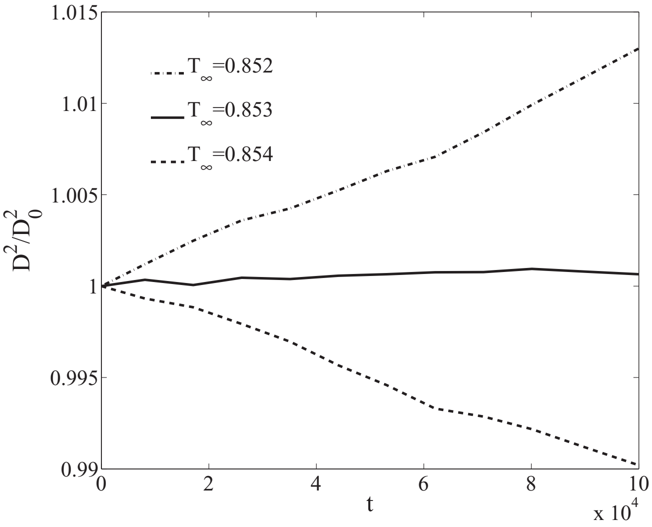

FIG. 6. Droplet size behavior for Re = 60 and different inlet temperature T_∞.

before evaporation is analyzed. Figure 6 shows the normalized square diameter evolution in time for different T_∞. When $T_\infty = 0.853$, the droplet size is nearly constant, i.e., close to a thermodynamic equilibrium. If $T_\infty < 0.853$, then the swelling is observed, where condensation occurs, as seen for $T_\infty = 0.852$. Whereas an increase of temperature ($T_\infty = 0.854$) induces the droplet evaporation.

From this point onward, a superheated vapor is imposed at the inlet, where evaporation is controlled by the temperature difference $\Delta T = T_\infty - T^*_{\text{sat}}$, with $T^*_{\text{sat}} = 0.853$, according to Fig. 6. The droplet shrinkage for different ΔT is illustrated in Fig. 7. The vapor generated from phase change convects and diffuses away from the droplet surface. As temperature is increased, stronger vaporization occurs and the droplet shrinks faster, where the lifetime is reduced.

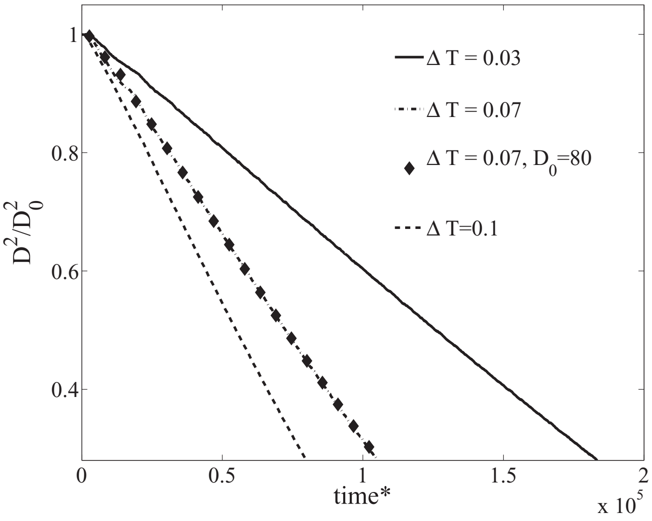

FIG. 7. Normalized square diameter as function of time for Re = 60 and different ΔT, where an increase of ΔT has an outcome of decreasing the droplet lifetime.

The grid convergence under convective effects is also investigated. In order to do so, the evaporation of an initial droplet size $D_{0(2)} = 80$ is compared to the reference $D_{0(1)} = 60$. A different inlet velocity is set according to $U_{(2)} = U_{(1)}D_{0(1)}/D_{0(2)}$ to achieve the same Re. The interface thickness change is proportional to the diameter ratio, i.e., $l_{i(2)} = l_{i(1)}D_{0(2)}/D_{0(1)}$, where $\kappa = 0.0075$ for $D_{0(2)} = 80$. Assuming the reference time scale as $t_{(1)} = D_{0(1)}/U_{(1)}$, $t_{(2)}$ is rescaled following $t_{(2)} = D_{0(2)}U_{(1)}/[D_{0(1)}U_{(2)}]$. The temperature difference is set as $\Delta T = 0.07$ and results are also shown in Fig. 7. Excellent agreement is seen between both droplet resolutions.

C. Oscillatory evaporation

In this section we employ a stronger flow to investigate the droplet evaporation dynamics. The Reynolds number is raised to Re = 130, where the Peclet number is Pe = 105. Again, a careful observation of the equilibrium condition is needed once the flow is imposed, where we must first find an appropriate T^*_{sat}. From this point onward the evaporation is described in terms of the normalized area A/A_0, since the droplet may exhibit slight deviations from a circular shape. Figure 8 shows A/A_0 evolution in time for different inlet temperatures. It is seen that the droplet has an oscillatory behavior. The droplet oscillates around its initial area for the plot $T_\infty = 0.86$, which is taken as T^*_{sat}. Larger values induce droplet evaporation while lower cause droplet swelling, as seen in the latter section, for lower Re.

It is important to understand the characteristics and mechanism of the droplet oscillations. Jangi and Kobayashi [55] studied the droplet evaporation for oscillatory flow, where a sinusoidal wave was established for the surrounding air. However, in the present case, the flow is uniform and oscillations are due to the wake-droplet interactions.

Figure 9 shows the streamlines for a region of the domain where there is wake formation, when $T_\infty = 0.86$ ($\Delta T = 0$). One period of oscillation is observed and the shape deformation $\delta_D = (D_x - D_y)/(D_x + D_y) \times 100$ is also

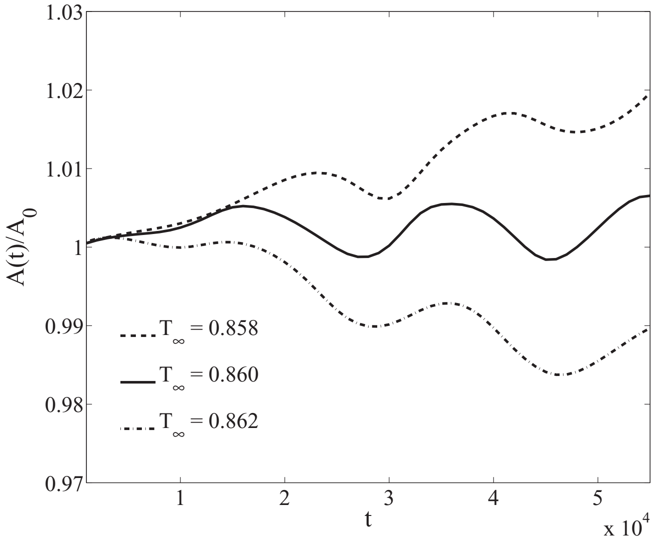

FIG. 8. Area as a function of time for different T_∞, where Re = 130 and oscillatory behavior is observed.

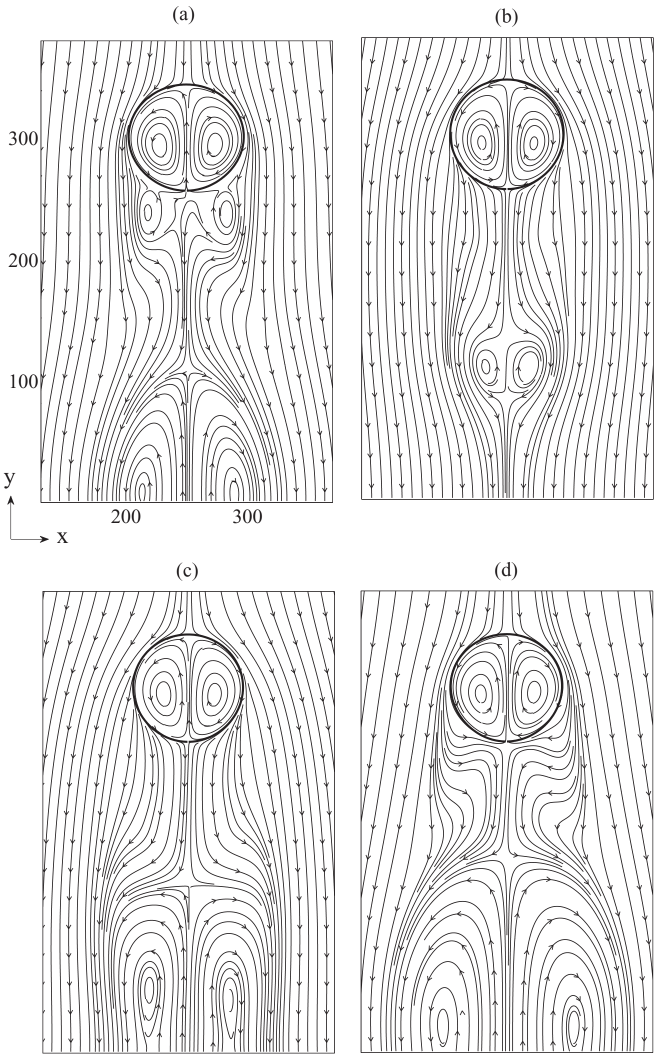

FIG. 9. Streamlines for Re $= 130$ and $\Delta T = 0$, as for the plot in Fig. 8. (a) $t = 3.12 \times 10^4$ ($\delta_D = 4.5\%$); (b) $t = 3.61 \times 10^4$ ($\delta_D = 1.8\%$); (c) $t = 4.15 \times 10^4$ ($\delta_D = 1.1\%$); (d) $t = 4.55 \times 10^4$ ($\delta_D = 1.8\%$).

considered, where D_x and D_y are the droplet width and breadth, respectively. In Fig. 9(a) it is seen that the flow separates at the droplet rear, where two symmetric eddies are formed. The evaporation rate, given as dA/dt is positive (i.e., condensation occurs) and maximum, where the deformation is $\delta_D = 4.5\%$. As it evolves in time, there is blowing at the bottom of the surface which induces the detachment of the vortices. These are convected along with the vapor flow, as seen in Fig. 9(b), where $dA/dt \cong 0$. Further on, the net blowing counteracts the condensation and evaporation is obtained (i.e., $dA/dt < 0$). The vortices develop and grow in size [Fig. 9(c)]. The evaporation rate dA/dt is at its minimum, where the deformation is lower $\delta_D = 1.1\%$. In Fig. 9(d) the vortices reach a maximum size and separation again starts taking place at the rear region of the droplet. The evaporation rate again assumes $dA/dt = 0$, where condensation is initiated. The cycle is completed with a similar configuration as in Fig. 9(a) where new vortices are again created while the ones blown away from the droplet are still leaving the domain at the outflow boundary. One should note that the larger vortices generate a backflow that causes a decrease of the blowing at the rear droplet which will reduce the pressure and assist the condensation at the bottom region. We also observed that at the crest and trough of the period [Figs. 9(b) and 9(d)] the same deformation is found, $\delta_D = 1.8\%$, where $dA/dt = 0$.

Smooth evaporation can be analyzed to show the difference between the evaporation and condensation scenarios. Figure 10 illustrates the isotherms along with velocity vectors normal to the droplet surface $\mathbf{v}_n$ for different times in Fig. 8, for the curve $T_\infty = 0.862$, which corresponds to $\Delta T = 0.002$. We choose the time in Fig. 10(a) as $t = 3.1 \times 10^4$ and (b) $t = 4.2 \times 10^4$, which correspond to the maximum and minimum evaporation rate of an oscillatory period, i.e., $dA/dt = 0$. A vector pointing outwards means that local evaporation occurs while if pointing inwards condensation takes place. It is seen in Fig. 10(a) that vapor enters at the top-bottom regions of the droplet, i.e., condensation takes place.

In Fig. 10(a) we observe an elongation in the x direction, where the deformation is $\delta_D = 3.1\%$. On the other hand, Fig. 10(b) shows condensation only at the rear part of the droplet and deformation $\delta_D = 0.9\%$ decreases. It is important to note that the droplet is still at an early stage of evaporation, i.e., near the equilibrium condition. One should also note that as ΔT is small, the internal heat-up is not significant. The increase of ΔT induces evaporation also at the front region, where the stagnation point may shift from droplet surface to the droplet forefront. In such a case, deformation is negligible, where $\delta_D \rightarrow 0$.

The isotherms exhibit a parabolic shape in Fig. 10(a), whereas in Fig. 10(b) a stronger effect of internal circulation is observed. We should point out that this difference is also related to the wake. In Figure 10(a) vortices are located around the droplet rear [as seen in Fig. 9(a)]. These are responsible for the occurrence of condensation and changes in pressure and therefore temperature. On the other hand, Fig. 10(b) exhibits a wake as seen in Fig. 9(c) where vortices are already detached and no separation is found along the droplet surface.

Local mass flow rate $J_m = \rho_i \mathbf{v}_n$ is quantified in Fig. 11, plotted along the surface, between 0 (top of the droplet) and π (bottom of the droplet), in radians. While condensation is dominant for $t = 3.1 \times 10^4$ at the top region (along 0 to 1 radians) and $J_m(0.2) = -4 \times 10^{-3}$, a stronger evaporation is identified when $t = 4.2 \times 10^4$, which takes place between 0.75 and π with a maximum $J_m(1.7) \cong 3 \times 10^{-3}$.

Figure 12 illustrates the tangential velocities $\mathbf{v}_t$ along the droplet surface. We observe a higher $\mathbf{v}_t$ when $t = 3.1 \times 10^4$, located at 1.2 rad. The boundary layer (BL) thickness in this case is 4.9 (l.u.), whereas for $t = 4.2 \times 10^4$ the thickness is 6.6 (l.u.). The widening of the BL when $t = 4.2 \times 10^4$ is due to the normal velocity component which is responsible for the blowing along the droplet surface. Therefore, one should note that if ΔT is raised and stronger evaporation is obtained, shear stresses are lowered due to the blowing effect and the BL is thicker.

Figure 13 illustrates the evaporation for Re $= 130$ and different ΔT. As ΔT increases the droplet lifetime is shortened, as expected. We note that both $\Delta T = 0.03$ and $\Delta T = 0.07$

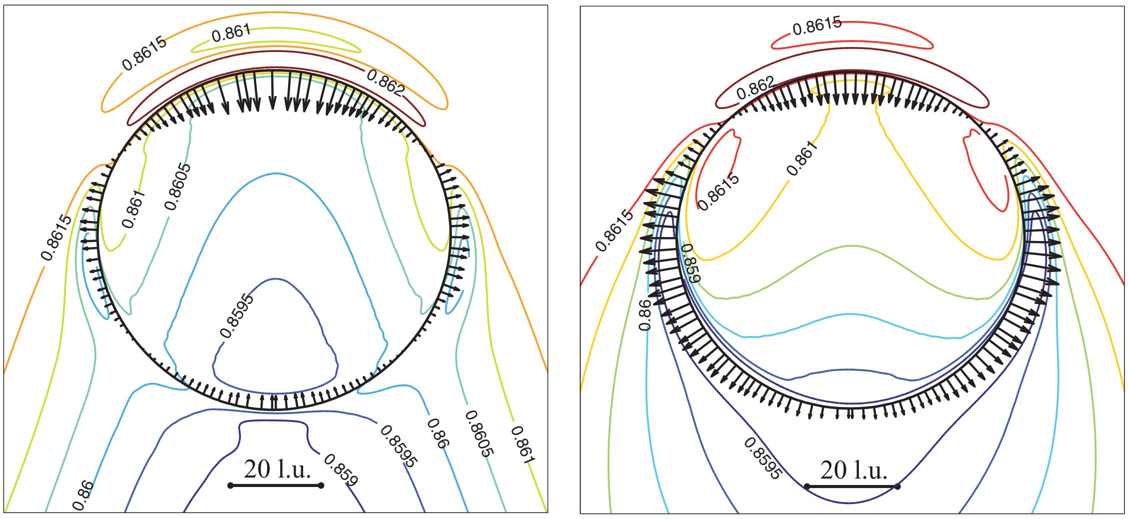

FIG. 10. (Color online) Isotherms and velocity vectors normal to the droplet surface, for Re = 130 and $\Delta T = 0.002$, where (a) $t = 3.1 \times 10^4$ (condensation) and (b) $t = 4.2 \times 10^4$ (evaporation).

show droplet oscillations that are attenuated. Once the heat exchange is enhanced, the blowing at the rear of the droplet is stronger and inhibits separation, i.e., further formation of eddies. Moreover, the influence of the backflow is lessened, once the blowing contributes to a faster convection of the vortices and the time scale for their development is reduced. It is also seen from Fig. 13 that for $A/A_0 < 0.8$ the evaporation rate is nearly constant where Re is reduced since it is linearly proportional to the droplet diameter.

A direct effect of increasing Re can be seen by comparing Fig. 13 to Fig. 7. For the same $\Delta T = 0.07$, we observe that the time taken for reaching $D^2/D_0^2 = 0.4$ is $t = 8.5 \times 10^4$ for Re = 60 and $t = 4.8 \times 10^4$ for Re = 130. The stronger convection is responsible for increasing the droplet internal circulation. Therefore, the exchange of heat between the droplet surface and the interior is enhanced due to the internal circulation.

IV. CONCLUSIONS

We have performed numerical simulations of droplet evaporation with forced convection using a lattice Boltzmann method. The phase change is set by a nonideal EOS which is incorporated in the interparticle potential force. The flow is solved using an MRT collision operator with the EDM forcing scheme implemented in the velocity space. Our approach makes use of double distribution functions, where the energy equation is solved as a separate distribution function and temperature is taken as a passive scalar.

Numerical simulations of a static droplet are used for validation. It is found that the method shows good agreement with the well-known D^2 law that prescribes the evaporation rate. The inclusion of convection alters the equilibrium conditions and the saturation point is adjusted according to the value of the Reynolds number. The evaporation rate is seen to increase when convection is stronger, as the internal

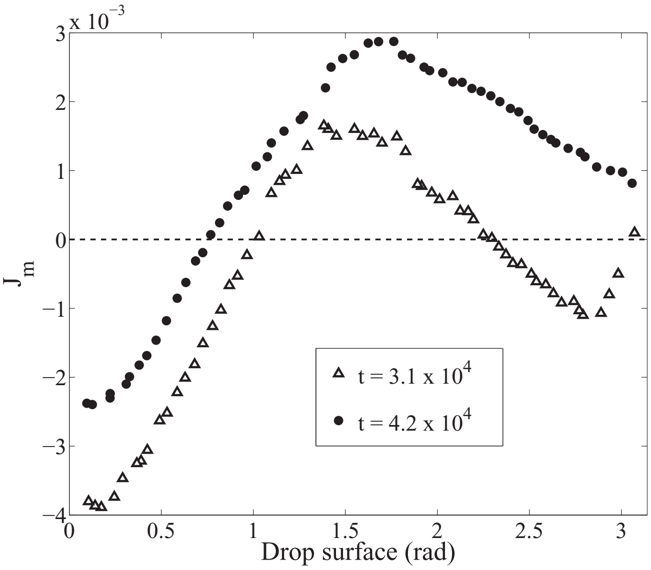

FIG. 11. Local mass flow rate in normal direction along the droplet surface for Re = 130 and $\Delta T = 0.002$.

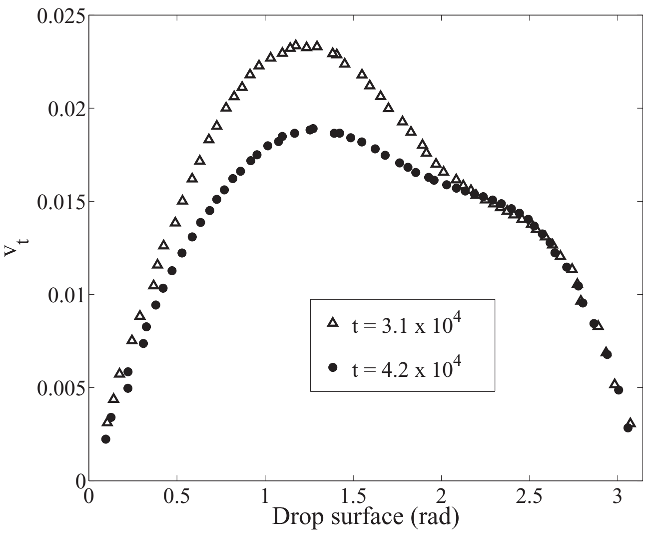

FIG. 12. Velocity in tangential direction along the droplet surface for Re = 130 and $\Delta T = 0.002$.

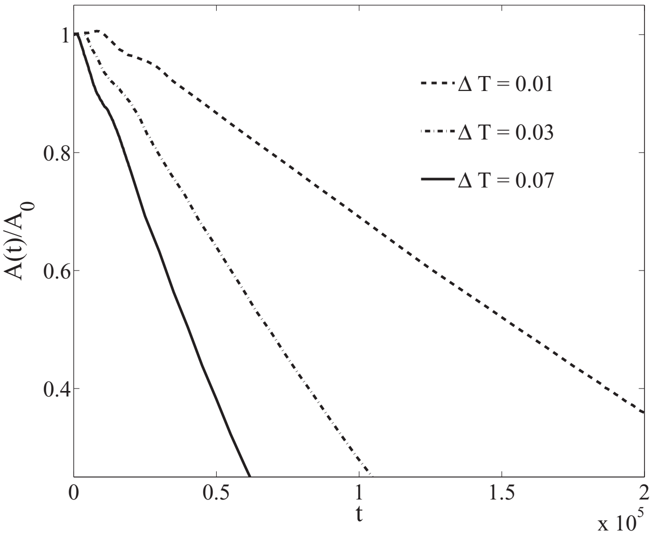

FIG. 13. Droplet evaporation for Re = 130 and different ΔT.

circulation enhances heat transfer. Raising the superheated vapor temperature decreases the droplet lifetime, as expected.

For higher Reynolds and Peclet numbers, the droplet exhibits an oscillatory behavior, where condensation and evaporation alternate. The wake-droplet interaction is the mechanism responsible for such oscillations and is investigated in detail. First, two symmetric eddies are formed at the droplet bottom region due to the flow separation, where the droplet deformation is maximum. The blowing along the droplet surface induces the detachment of these vortices, which are convected along with the vapor flow. At this point the droplet deformation is minimum. As the vortices grow in size, a backflow is generated which assists the formation of new eddies close to the droplet rear region, completing an oscillatory cycle. When the temperature difference increases and diffusion plays a major role we observe that the blowing inhibits further formation of eddies and droplet deformation is negligible. Therefore, the oscillations are attenuated and the evaporation rate is nearly constant for $A/A_0 < 0.8$. In addition, the local mass flow rate along the surface is also quantified and it is shown that a wider boundary layer is obtained when blowing occurs as shear stresses are decreased. In a future work, we will extend the method to three-dimensional and investigate different droplet breakups with evaporation.

ACKNOWLEDGMENTS

The financial support of the Swedish Research Council (VR2010-3938 and VR2011-5355) the computation time provided by the Swedish National Infrastructure for Computing (SNIC) and the pan-European HPC Research Infrastructure (PRACE-3IP, project FP7 RI-312763) are highly appreciated.

---

[1] M. Renksizbulut and M. C. Yuen, J. Heat Transfer **105**, 389 (1983).
[2] M. Renksizbulut and R. J. Haywood, Int. J. Multiphase Flow **14**, 189 (1998).
[3] R. J. Haywood, M. Renksizbulut, and G. D. Raithby, Int. J. Heat Mass Transfer **37**, 1401 (1994).
[4] S. Tanguy, T. Menard, and A. Berlemont, J. Comput. Phys. **221**, 837 (2007).
[5] H. Zhang, Combust. Sci. Technol. **175**, 2237 (2003).
[6] B. Balaji, V. Raghavan, K. Ramamurthi, and G. Gogos, Phys. Fluids **23**, 063601 (2011).
[7] M. Hase and B. Weigand, *High Performance Computing in Science and Engineering '03* (Springer-Verlag, Berlin, 2003), pp. 255–266.
[8] M. Hase and B. Weigand, Int. J. Numer. Methods Heat Fluid Flow **14**, 85 (2004).
[9] J. Schlottke and B. Weigand, J. Comput. Phys. **227**, 5215 (2008).
[10] G. Strotos, M. Gavaises, A. Theodorakakos, and G. Bergeles, Fuel **90**, 1492 (2011).
[11] R. Banerjee, Fuel **107**, 724 (2013).
[12] S. S. Sazhin, Prog. Energy Combust. Sci. **32**, 162 (2006).
[13] H. Y. Erbil, Adv. Colloid Interface Sci. **170**, 67 (2012).
[14] L. N. Long, M. M. Micci, and B. C. Wong, Comput. Phys. Commun. **96**, 167 (1996).
[15] J. H. Walther and P. Koumoutsakos, J. Heat Transfer **123**, 741 (2001).
[16] L. Consolini, S. K. Aggarwal, and S. Murad, Int. J. Heat Mass Transfer **46**, 3179 (2003).
[17] S. Sumardiono and J. Fischer, Microfluid. Nanofluid. **3**, 127 (2007).
[18] E. S. Landry, S. Mikkilineni, M. Paharia, and A. J. H. McGaughey, J. Appl. Phys. **102**, 124301 (2007).
[19] R. Holyst, M. Litniewski, D. Jakubczyk, K. Kolwas, and M. Kolwas, Rep. Prog. Phys. **76**, 034601 (2013).
[20] S. Chen and G. D. Doolen, Annu. Rev. Fluid Mech. **30**, 329 (1998).
[21] X. Shan and H. Chen, Phys. Rev. E **47**, 1815 (1993).
[22] A. L. Kupershtokh and D. A. Medvedev, J. Electrostat. **64**, 581 (2006).
[23] S. Gong and P. Cheng, Comput. Fluids **53**, 93 (2012).
[24] P. L. Bhatnagar, E. P. Gross, and M. Krook, Phys. Rev. **94**, 511 (1954).
[25] P. Lallemand and L. S. Luo, Phys. Rev. E **61**, 6546 (2000).
[26] P. Lallemand and L. S. Luo, Phys. Rev. E **68**, 036706 (2003).
[27] R. Zhang and H. Chen, Phys. Rev. E **67**, 066711 (2003).
[28] A. Márkus and G. Házi, Phys. Rev. E **83**, 046705 (2011).
[29] M. Sbragaglia, R. Benzi, L. Biferale, H. Chen, X. Shan, and S. Succi, J. Fluid Mech. **628**, 299 (2009).
[30] G. Gonnella, A. Lamura, and V. Sofonea, Phys. Rev. E **76**, 036703 (2007).
[31] Y. Gan, A. Xu, G. Zhang, P. Zhang, and Y. Li, Europhys. Lett. **97**, 44002 (2012).
[32] B. J. Palmer and D. R. Rector, Phys. Rev. E **61**, 5295 (2000).
[33] B. J. Palmer and D. R. Rector, Phys. Rev. E **69**, 049903 (2004).
[34] H. Safari, M. H. Rahimian, and M. Krafczyk, Phys. Rev. E **88**, 013304 (2013).

[35] R. Ledesma-Aguilar, D. Vella, and J. M. Yeomans, Soft Matter **10**, 8267 (2014).

[36] M. E. McCracken and J. Abraham, Phys. Rev. E **71**, 036701 (2005).

[37] Q. Li, K. H. Luo, and X. J. Li, Phys. Rev. E **87**, 053301 (2013).

[38] D. Lycett-Brown and K. H. Luo, Comput. Math. Appl. **67**, 350 (2014).

[39] X. He, S. Chen, and G. D. Doolen, J. Comput. Phys. **146**, 282 (1998).

[40] X. Shan, X. F. Yuan, and H. Chen, J. Fluid Mech. **550**, 413 (2006).

[41] A. J. Wagner, Phys. Rev. E **74**, 056703 (2006).

[42] P. Yuan and L. Schaefer, Phys. Fluids **18**, 042101 (2006).

[43] A. L. Kupershtokh, D. A. Medvedev, and D. I. Karpov, Comput. Math. Appl. **58**, 965 (2009).

[44] D. Jacqmin, J. Fluid. Mech. **402**, 57 (2000).

[45] M. R. Kamali, J. J. J. Gillissen, H. E. A. van den Akker, and S. Sundaresan, Phys. Rev. E **88**, 033302 (2013).

[46] H. Liu and Y. Zhang, J. Comput. Phys. **229**, 9166 (2010).

[47] I. Ginzburg, Adv. Water Resour. **28**, 1171 (2005).

[48] J. Wang, D. Wang, P. Lallemand, and L. Luo, Comp. Math. Appl. **65**, 262 (2013).

[49] H. Liu, A. J. Valocchi, Y. Zhang, and Q. Kang, Phys. Rev. E **87**, 013010 (2013).

[50] D. L. Albernaz, M. Do-Quang, and G. Amberg, Interfac. Phenom. Heat Transfer **1**, 245 (2013).

[51] W. A. Sirignano, *Fluid Dynamics and Transport of Droplet and Sprays* (Cambridge University Press, New York, 2010).

[52] K. K. Y. Kuo, *Principles of Combustion* (John Wiley & Sons, New York, 2005).

[53] E. W. Lemmon, M. O. McLinden, and D. G. Friend, *Thermophysical Properties of Fluid Systems in NIST Chemistry WebBook*, NIST Standard Reference Database Number 69 (National Institute of Standards and Technology, Gaithersburg, 2013).

[54] A. E. Komrakova, D. Eskin, and J. J. Derksen, Phys. Fluids **25**, 042102 (2013).

[55] M. Jangi and H. Kobayashi, Int. J. Heat Fluid Flow **30**, 729 (2009).